

Efficient Quantum Circuit Simulation by Tensor Network Methods on Modern GPUs

FENG PAN*, CAS Key Laboratory for Theoretical Physics, Institute of Theoretical Physics, Chinese Academy of Sciences, China and Centre for Quantum Technologies, National University of Singapore, Singapore

HANFENG GU*, NVIDIA, China

LVLIN KUANG, NVIDIA, China

BING LIU, NVIDIA, China

PAN ZHANG, CAS Key Laboratory for Theoretical Physics, Institute of Theoretical Physics, Chinese Academy of Sciences, China, School of Fundamental Physics and Mathematical Sciences, Hangzhou Institute for Advanced Study, UCAS, China, and International Center for Theoretical Physics Asia-Pacific, China

Efficient simulation of quantum circuits has become indispensable with the rapid development of quantum hardware. The primary simulation methods are based on state vectors and tensor networks. As the number of qubits and quantum gates grows larger in current quantum devices, traditional state-vector based quantum circuit simulation methods prove inadequate due to the overwhelming size of the Hilbert space and extensive entanglement. Consequently, brutal force tensor network simulation algorithms become the only viable solution in such scenarios. The two main challenges faced in tensor network simulation algorithms are optimal contraction path finding and efficient execution on modern computing devices, with the latter determines the actual efficiency. In this study, we investigate the optimization of such tensor network simulations on modern GPUs and propose general optimization strategies from two aspects: computational efficiency and accuracy. Firstly, we propose to transform critical Einstein summation operations into GEMM operations, leveraging the specific features of tensor network simulations to amplify the efficiency of GPUs. Secondly, by analyzing the data characteristics of quantum circuits, we employ extended precision to ensure the accuracy of simulation results and mixed precision to fully exploit the potential of GPUs, resulting in faster and more precise simulations. Our numerical experiments demonstrate that our approach can achieve a 3.96x reduction in verification time for random quantum circuit samples in the 18-cycle case of Sycamore, with sustained performance exceeding 21 TFLOPS on one A100. This method can be easily extended to the 20-cycle case, maintaining the same performance, accelerating by 12.5x compared to the state-of-the-art CPU-based results and 4.48-6.78x compared to the state-of-the-art GPU-based results reported in the literature. Furthermore, the strategies presented in this article hold general applicability for accelerating problems that can be tackled by contracting tensor networks such as graphical models and combinatorial optimizations.

Additional Key Words and Phrases: quantum computing, quantum circuit simulation, tensor network, GPU

*Both authors contributed equally to this research.

Authors' addresses: Feng Pan, CAS Key Laboratory for Theoretical Physics, Institute of Theoretical Physics, Chinese Academy of Sciences, Beijing, China, 100190 and Centre for Quantum Technologies, National University of Singapore, 117543, Singapore, fengpan1994@gmail.com; Hanfeng Gu, NVIDIA, Shanghai, China, henrygu@nvidia.com; Lvlin Kuang, NVIDIA, Beijing, China, lkuang@nvidia.com; Bing Liu, NVIDIA, Shenzhen, China, petrickl@nvidia.com; Pan Zhang, CAS Key Laboratory for Theoretical Physics, Institute of Theoretical Physics, Chinese Academy of Sciences, Beijing, China, 100190 and School of Fundamental Physics and Mathematical Sciences, Hangzhou Institute for Advanced Study, UCAS, Hangzhou, Zhejiang, China, 310024 and International Center for Theoretical Physics Asia-Pacific, Beijing/Hangzhou, China, panzhang@itp.ac.cn.

Permission to make digital or hard copies of all or part of this work for personal or classroom use is granted without fee provided that copies are not made or distributed for profit or commercial advantage and that copies bear this notice and the full citation on the first page. Copyrights for components of this work owned by others than ACM must be honored. Abstracting with credit is permitted. To copy otherwise, or republish, to post on servers or to redistribute to lists, requires prior specific permission and/or a fee. Request permissions from permissions@acm.org.

© 2023 Association for Computing Machinery.

Manuscript submitted to ACM

ACM Reference Format:

Feng Pan, Hanfeng Gu, Lvlin Kuang, Bing Liu, and Pan Zhang. 2023. Efficient Quantum Circuit Simulation by Tensor Network Methods on Modern GPUs. 1, 1 (October 2023), 25 pages. <https://doi.org/10.1145/nnnnnnnn.nnnnnnnn>

1 INTRODUCTION

Quantum computing is a rapidly developing interdisciplinary field that combines concepts from physics and computer science. Unlike classical computers, which rely on binary bits, quantum computers use quantum mechanical systems constructed by qubits that hold the power of superpositions and entanglement. This potential of quantum computing allows to solve certain problems polynomially or exponentially faster than classical computing, making it a competitive challenger to the extended Church-Turing thesis and a promising candidate for post-Moore computation.

The concept of quantum computing was first introduced by pioneers such as Feynman in the 1980s [16]. Since then, quantum computers have been built in various platforms. However, in the current Noisy Intermediate-Scale Quantum (NISQ) era [45], several tasks with rigorous theoretical foundations, such as factoring [47] and database searching [19], cannot be executed on current quantum devices without the assistance of quantum error correction.

To identify possible gaps between quantum and classical computing on noisy quantum devices, researchers have focused on sampling-based quantum computing tasks, such as Gaussian Boson sampling (GBS) [1, 21] and Random Quantum Circuit Sampling (RCS) [2, 9]. The noise-free versions of these tasks have been proven to be exponentially hard for classical computation. Several quantum hardware systems have achieved these computational tasks [6, 30, 51, 52, 54]. Their results indicate quantum computational advantages over specific classical algorithms run on state-of-the-art supercomputers.

The claim of quantum computational advantage based on RCS experiments on NISQ devices has been disputed since Google claimed in 2019 [6] that classical simulation of their 53-qubit, 20-cycle Sycamore circuits would take supercomputers 10,000 years. The Linear Cross-Entropy Benchmark (LXEB), which determines the fidelity of their sampling results, has been targeted by several spoofing algorithm [7, 17, 42], due to the extremely low LXEB value of Sycamore circuits (around 0.2%). Moreover, a recent seminal study has established that RCS experiments with a constant error rate per gate in the asymptotic limit are poly-time classically simulatable [4]. Although this algorithm cannot handle finite-size cases due to its exponentially growing coefficient with gate error rate, it has effectively disproven the possibility of an expanding quantum advantage in noisy quantum circuits with larger sizes.

In the meantime, classical simulation and verification of finite-size RCS experiments are also very crucial. Classical simulation involves sampling bitstrings with bounded LXEB values from quantum circuits, which helps to understand gaps between quantum and classical computing regarding this task. Classical verification, on the other hand, entails calculating the exact amplitudes sampled in the RCS experiments, serving two primary objectives. Firstly, it validates the authentic outputs of the RCS experiments, thus ensuring the reliability of the experimental results. Secondly, efficient verification methods enable the realization of numerous potential applications of such sampling-based quantum algorithms, such as solving subgraph problems [5] and generating random numbers with certified randomness [3, 8].

Classical simulation and verification techniques for quantum algorithms have traditionally relied on state vector based methods. However, they are only practical for circuits with a limited number of qubits, where it is possible to store the entire state vector or density matrix. For quantum circuits with low entanglement, state vectors can be accurately approximated and efficiently operated [12, 53]. These approaches result in a polynomial computational cost and enable simulation of larger system sizes. However, when attempting to perform classical simulations of quantum algorithms

that demonstrate quantum computational advantages, these methods fail due to the large number of qubits (usually greater than 50) and high-entanglement circuit architecture.

A practical way to simulate such quantum experiments is the brutal force tensor network simulation algorithm [33]. This method converts all components of the quantum circuit into tensor networks, which are then contracted to obtain specific final state bitstring amplitudes. Although this approach can handle cases with a large number of qubits and high entanglement, it still faces several challenges, with two core ones being the contraction path finding and efficient implementation on current classical devices.

Due to the substantial number of tensors involving multiple dimensions within the tensor network simulation, identifying an optimal contraction path presents an immensely challenging combinatorial optimization problem with no known efficient heuristic algorithm. Recently, various path-finding approaches employing graph-partitioning, simulated-annealing-like, and architecture-aware methods [11, 18, 22, 41, 42] have demonstrated significant advancements in the bounded-fidelity simulation of RCS experiments [22, 29, 41]. These advancements have significantly improved the simulation time for a 53-qubit, 20-cycle Sycamore circuit, reducing the original estimated time of 10,000 years in Google’s paper to a duration comparable to quantum experiments.

Furthermore, achieving an efficient implementation of such tensor network simulation tasks poses a non-trivial challenge, as modern high-performance computing devices are not specifically designed to handle tensor contractions with the arbitrariness of dimension and contraction indices, and the computational tasks require a substantial amount of both computing capacity and memory speed. Previous studies [22, 25, 28, 29, 41] indicate that current implementations only utilize around 20% of the peak performance of the devices. Considering that the verification tasks are considerably more arduous than the bounded-fidelity simulation tasks, achieving a much more efficient implementation on modern devices is imperative.

The main focus of this paper is on the optimization of tensor network methods used in simulating and verifying quantum circuit-based experiments, with a view to making them more efficient on modern GPUs. Specifically, we optimize the simulation method proposed in [41], and target RCS experiments. The contributions of our work can be summarized as follows:

- We devise a strategy that transfers the most time-consuming component of the sparse-state tensor network simulation from sparse Einstein summation (einsum) to GEMM operations. This optimization results in a significant decrease in the overall running time of that component.
- We undertake an in-depth investigation of the impact of data types on the simulation results of quantum circuits. We propose a scheme that employs different precisions in different simulation stages. This approach leverages Tensor Cores on modern GPUs while ensuring accuracy and consistency of simulation results.
- We conduct extensive numerical experiments to test our optimization strategies. With the use of NVIDIA A100 GPUs, we successfully verify RCS experiments based on 53-qubit 18-cycle Sycamore circuits with 2^{20} sampled bitstrings, using 8435 GPU hours. This is 3.96 times faster than the non-optimized version. Moreover, for 53-qubit 20-cycle Sycamore circuits with three million sampled bitstrings verification task, the estimated computational resource is 1.26 million GPU hours. This is 12.5 times faster than the supercomputer’s time reported in [28], assuming the same single-precision peak performance is maintained. Using the proposed methodology, we could also achieve the simulation task of bounded LXEB value (0.2%), at an estimated computational cost of 2819 GPU hours. Compared to the results reported in [25] and [41] with the same computing complexity, the simulation could be accelerated by 4.48 and 6.78 times, respectively.

It is worth noting that the algorithm employed in this study does not determine the number of qubits, the types of two-qubit gates, or the quantum circuit connections. As a result, the optimizations described in this article are generalizable to any quantum circuits and any quantum circuit based algorithm [15, 43], with the circuits used in random circuit sampling representing particularly challenging cases. Furthermore, these optimizations can be extended to address other problems that involve tensor network contractions, including graphical models [46], combinatorial optimization problems [26], quantum error correction [10], and so forth.

The remainder of the paper is structured as follows: Section 2 provides an overview of quantum circuit models, tensor networks, RCS experiments, and simulations on GPUs. In Section 3, we provide a detailed description of the algorithms we employ to leverage tensor network contractions for simulating quantum circuits. Section 4 presents a comprehensive explanation of the enhancements we introduce to the tensor network simulation to significantly enhance its efficacy on modern GPUs. In Section 5, we assess the performance of the optimized tensor network simulation and compare it to other implementations. We wrap up the study by discussing our conclusions and future research directions in Section 6.

2 BACKGROUND

2.1 Quantum circuits and Tensor Network Simulation

Quantum circuits, like their classical counterparts, are circuits made up of quantum gates. In contrast to classical circuits that utilize high and low voltages to represent binary states, quantum circuits use quantum superposition to encode multiple classical states at the same time. The interaction and manipulation of quantum states are governed by unitary operations called quantum gates. To extract information encoded within quantum states, measurements are performed. The result of a measurement is a collapsed 0-1 bitstring in the measurement basis. It is noteworthy that measurements destroy the superposition of quantum states. Thus, repetition of the entire experiment is necessary to gain more information regarding the quantum state.

Quantum gates and initial quantum states can be mathematically represented by tensors and vectors, respectively. The interconnection and ordering of quantum gates and quantum states in quantum circuits can be mapped to the bonds between tensors. This mapping enables the conversion of a quantum circuit into a unique tensor network. Given a separable initial state, the tensor network input is closed in the initial state section and opened in the final state section. The open bonds found in this area indicate the configurations of individual qubits. By contracting the tensor network, we may acquire a vector that combines all open bonds into a singular entity. This vector comprises the final quantum state of the circuit and contains all amplitudes of the entire Hilbert space. An illustration of a tensor network representation of a quantum circuit is shown in Figure 2(a).

The measurement process in quantum circuits lacks a corresponding tensor network methodology for large-scale quantum circuits. This is due to the fact that the quantum state vector cannot be stored in its entirety by any classical computer when the number of qubits surpasses 50. As a result, it is impossible to generate samples from it. For tensor network simulations, even though the entire state vector cannot be retrieved, the amplitudes of small sets of bitstrings can be obtained. By utilizing these bitstrings and their corresponding probabilities, sampling approaches such as importance sampling or rejection sampling can be employed to extract samples from them. This process captures the measurement process of quantum experiments [9, 22].

2.2 Random Quantum Circuit Sampling Experiments

RCS experiments[2, 6, 9, 51, 54] execute multiple measurements on the final state of a random quantum circuit, generating bitstring samples that align with a specific distribution called the Port-Thomas distribution [44] of that final state. The construction of the quantum circuit is typically achieved by organizing sequences of quantum gates, with each sequence composed of a single-qubit gate layer, followed by a two-qubit gate layer. The entire circuit is comprised of numerous such cycles.

In order to make classical simulation difficult, two-qubit quantum gates are carefully designed to be full rank in the temporal direction within random quantum circuits. This design choice increases classical complexity. The quantum circuit's randomness comes from the utilization of a specific gate set for single-qubit gates, which are randomly selected. In the designs of two quantum circuits that have demonstrated quantum computational advantage [6, 51, 54], fermionic simulation (fsim) gates with carefully tuned parameters are used as two-qubit gates, while single-qubit gates are selected randomly from the \sqrt{X} , \sqrt{Y} , and \sqrt{W} gates.

Upon obtaining the sampled bitstrings, a LXEB procedure is then executed to evaluate the quality of said samples. LXEB is introduced as a viable substitute for the actual fidelity, which is practically difficult to obtain in quantum circuits that involve a large number of qubits. The LXEB equation is,

$$F_l = 2^N \sum_x p_U(x)q(x) - 1 = 2^N \mathbb{E}_{x \sim q(x)} p_U(x) - 1, \quad (1)$$

where N is the number of qubits in the quantum circuit, x denotes the bitstring, and the summation is performed over all possible bitstrings. $p_U(x)$ represents the probability of said bitstring in the ideal circuit that is devoid of noise, and $q(x)$ represents the probability of said bitstring in the real circuit.

However, in real-world quantum experiments, obtaining a complete ensemble of bitstrings for the evaluation of $q(x)$ and calculation of its associated expectation value is infeasible. Therefore, a set number of bitstrings are randomly sampled, with the LXEB subsequently computed as

$$F_l = 2^N \sum_{i=1}^m p_U(x_i)/m - 1. \quad (2)$$

It is worth noting that $p_U(x_i)$ should be calculated using classical computation, but due to the difficulty of calculating it, quantum experiments will be done in simplified circuits which can be simulated efficiently in classical computers. The circuits for demonstration of quantum computational advantages only differ in their choice of two-qubit gates, allowing LXEB values to be inferred from those of simpler circuits.

Quantum hardware has demonstrated the capacity to perform RCS experiments with a high level of efficiency. A single instance of quantum state preparation and measurement can be completed in a mere few milliseconds. The Sycamore circuits, for example, required approximately 600 seconds to sample 3 million bitstrings, with a final LXEB of 0.224%. The largest Zuchongzhi circuit, by contrast, necessitated 4.2 hours to sample 70 million bitstrings, but exhibited a final LXEB of 0.0366%.

2.3 Modern GPU

Modern GPUs are SIMD architectures that break down computing tasks into thousands of threads for parallel execution, making it highly suitable for compute-intensive tasks. The bandwidth of GPU memory can typically reach TB/s levels,

Table 1. Floating-point format and peak performance on A100 GPU

| Floating Precision | FP64 | FP32 | TF32 | FP16 | BF16 |
|---------------------|-------|------|------|------|------|
| Sign Bits | 1 | 1 | 1 | 1 | 1 |
| Exponent Bits | 11 | 8 | 8 | 5 | 8 |
| Mantissa Bits | 52 | 23 | 10 | 10 | 7 |
| Range Min | E-308 | E-38 | E-38 | E-8 | E-38 |
| Range Max | E+308 | E+38 | E+38 | E+4 | E+38 |
| Significant Digits | 15~16 | 7~8 | 3~4 | 3~4 | 2~3 |
| CUDA Core(TFlops) | 9.7 | 19.5 | / | 78 | 39 |
| Tensor Core(TFlops) | 19.5 | / | 156 | 312 | 312 |

giving GPU a significant advantage in processing tasks that require high bandwidth. Additionally, modern GPU typically has large memory, which is crucial for tensor network contraction.

In modern GPU hardware represented by NVIDIA GPUs, the core computing unit is the streaming multiprocessor (SM), which contains CUDA Cores (FP64, FP32, INT32) and Tensor Cores. These units perform tasks in three parallel computing levels, grid, block, and thread. The grid is the largest unit, representing the entire program or task; the block is a subset of the grid, representing a group of threads that can collaborate; the thread is an element within the block, representing the smallest unit that executes specific instructions.

The Tensor Core, which was first introduced in the NVIDIA Tesla V100 GPU and further enhanced in recent NVIDIA Ampere and Hopper GPUs [13, 14], is a specialized unit for matrix multiplication and accumulation operations. For these operations, the Tensor Core is more efficient than the CUDA Core since the Tensor Core can perform multiple fused multiply-add (FMA) operations per clock cycle per instruction, while the CUDA Core can only perform one per clock cycle per instruction. Thus, the Tensor Core can provide up to 2–8x speedups compared to the CUDA Core (see Table 1). However, the Tensor Core has hardware limitations and can only process matrix operations of fixed sizes. To fully utilize the computing power of Tensor Cores, each dimension of the input matrix must be a multiple of 8 [37]. This requires branch merging [22] in tensor network contraction, as quantum gates (single-qubit or two-qubit) are usually represented as 2-way or 4-way tensors.

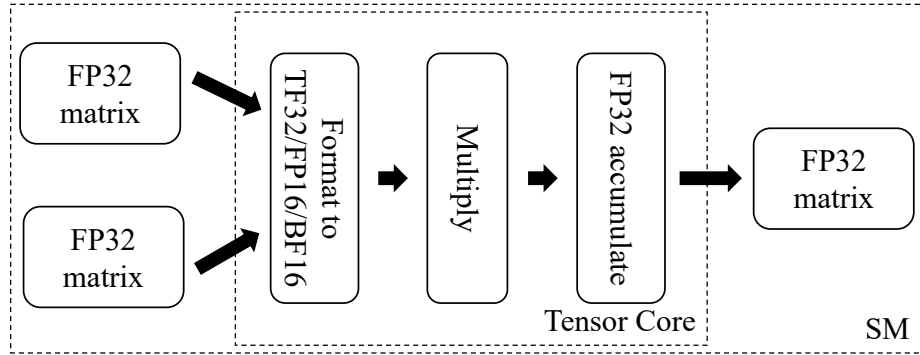


Fig. 1. FP32 input/output matrices multiplication using the Tensor Core (source: NVIDIA).

Another issue to consider when using Tensor Cores is precision. While Tensor Cores support FP64 in Ampere and subsequent architectures, it is beneficial to explore lower precision compute modes such as TF32, FP16, and BF16 to Manuscript submitted to ACM

attain higher performance. As shown in Table 1, the peak performance of TF32/FP16/BF16 is 8-16 times greater than that of FP32/FP64. To utilize the peak performance of TF32/FP16/BF16 format, Tensor Cores provide the function of converting high-precision inputs into low-precision formats during computation, and using single-precision format in the accumulation process and output format (see Figure 1). This can yield a highly favorable acceleration ratio while satisfying the precision requirements of applications such as artificial intelligence. Nevertheless, precision issues may arise when employing TF32/FP16/BF16 in precision-sensitive scientific computing, as their narrower exponent range or fewer significant digits compared to FP32/FP64 may lead to imprecision, necessitating careful consideration and remediation [31, 38, 39].

2.4 Efficient tensor contraction on GPU

Any dimensional tensor contraction can be expressed by a summation formula as follows:

$$C_{\gamma_1 \gamma_2 \dots \gamma_{d_C}} = \sum_{\delta_1} \sum_{\delta_2} \dots \sum_{\delta_{d_S}} A_{\alpha_1 \alpha_2 \dots \alpha_{d_A}} B_{\beta_1 \beta_2 \dots \beta_{d_B}} \quad (3)$$

where $\delta_1 \delta_2 \dots \delta_{d_S} = (\alpha_1 \alpha_2 \dots \alpha_{d_A}) \cap (\beta_1 \beta_2 \dots \beta_{d_B})$ are the contracting indices for both tensors A and B , which are summed, and

$$\gamma_1 \gamma_2 \dots \gamma_{d_C} = (\alpha_1 \alpha_2 \dots \alpha_{d_A}) \cup (\beta_1 \beta_2 \dots \beta_{d_B}) \setminus (\delta_1 \delta_2 \dots \delta_{d_S})$$

are the remaining indices for both tensors A and B . The dimensions of tensors A , B , and C are d_A , d_B , and d_C , respectively and d_S is the number of contracting indices.

The computing complexity (T_{cc}) of the tensor contraction

$$T_{cc} = \text{ops_per_element} * \prod_{i=1}^{d_A} \text{len}(\alpha_i) \prod_{i=1}^{d_B} \text{len}(\beta_i) / \prod_{i=1}^{d_S} \text{len}(\delta_i), \quad (4)$$

is the product of total dimensions of each tensor divided by the total dimension of the contracting indices. The term `ops_per_element` represents the number of floating-point operations required for the multiplication of elements, for example, `ops_per_element` = 8 for complex number multiplication.

The memory complexity (T_{mc}) for the contraction is the sum of the memory required to store the two input tensors A, B and the output tensor C

$$T_{mc} = \text{sizeof_data} * \left(\prod_{i=1}^{d_A} \text{len}(\alpha_i) + \prod_{i=1}^{d_B} \text{len}(\beta_i) + \prod_{i=1}^{d_C} \text{len}(\gamma_i) \right). \quad (5)$$

The term `sizeof_data` represents the number of bytes for an element. One important indicator to assess whether tensor contractions can leverage the performance of a GPU platform is the arithmetic intensity, which is defined as the ratio of T_{cc} and T_{mc} .

For high performance implementation of tensor contraction on GPU, the main difficulty lies in the arbitrariness of tensor dimension and tensor contraction indices. Generally speaking, there are two main ways to efficiently implement tensor contraction on GPU:

Transpose-Transpose GEMM Transpose (TTGT) contraction: The TTGT method mainly divides tensor contraction into two types of operations: tensor transpose and matrix-matrix multiplication (GEMM). The purpose of tensor transpose is to transfer a tensor of arbitrary dimension into a flat two-dimensional matrix, where the uncontracting indices are merged into one dimension and the contracting indices are merged into another dimension and vice versa.

In this way, the transposed tensor can be computed using the already highly optimized GEMM operation, and finally, the GEMM calculation result can be transposed back to the result tensor as needed. The advantage of this method is its versatility. The operation decomposition allows to utilize specialized transpose operation libraries (such as cuTT [23] and TTLG [50]) and GEMM libraries (such as cuBLAS and CUTLASS) separately on the GPU. However, this method also has obvious drawbacks: 1) Tensor transpose requires additional temporary space to store the transposed tensor, which is fatal in quantum circuit simulation because of its high memory requirement; 2) The arithmetic intensity of TTGT will be much lower compared to an equally-sized GEMM because each element needs to be loaded at least twice. **GEMM-like Tensor-Tensor (GETT)** contraction [48]: The GETT method is based on a cache-based hierarchical and size-unrolled tensor contraction loop, which explicitly loads sub-loops into each level of GPU cache. This avoids the need for explicit preprocessing steps and allows for operations on sub-tensors of any order while preserving memory access with stride 1. The advantages of this method are: 1) No need for explicit tensor transposition, avoiding additional temporary storage overhead; 2) Can preserve arithmetic intensity for any given tensor contraction compared to the equally-sized GEMM. The disadvantage is that optimized routines need to be implemented separately for each individual tensor contraction case. The GPU-accelerated tensor library cuTensor uses this method [49].

3 SIMULATION ALGORITHM

In this section, we will present the overall simulation algorithm. The purpose of the simulation method is to accurately calculate the amplitudes of sampled bitstrings from quantum experiments. The simulation method consists of three main steps: contraction path finding, dynamic slicing, and sparse-state contraction, which will be discussed in detail below.

3.1 Contraction path representations

A contraction path is a sequential order of tensors that are to be contracted at each step. In this study, we have limited our focus to the pairwise contraction approach, where two tensors are contracted at each step. For pairwise contractions, the contraction path's length for a N -tensor network is $N - 1$, where each position within the path specifies the indices of the tensors to be contracted. The contracted tensor resulting from each step is indexed by the first tensor to be processed.

Alternative representations of the contraction path can be useful for instructional purposes. One such representation is the contraction tree [18]. The contraction tree is a binary tree in which the leaf nodes signify the tensors to be contracted. The parent vertices of these leaf nodes correspond to the resulting tensor from each pairwise contraction operation. Once all the tensors have been contracted, the leaves of the tree are merged into a single root vertex, which represents the final tensor. Figure 2(a) and (b) depicts a tensor network and a possible contraction tree to contract it.

3.2 Path finding approach

Finding a contraction path through a tensor network is a challenging combinatorial optimization problem that depends on the sequence of operations. It is an NP-hard problem, and to date, there is no efficient algorithm available to solve it. However, significant progress has been made in recent years by leveraging graph partitioning tools to determine an optimal contraction order. [18] have demonstrated that this approach dramatically improves performance for a broad range of quantum circuits. The state-of-the-art algorithm used to solve this problem mimics the simulated annealing (SA) process [24]. By implementing a SA-like approach and defining local transformations of the contraction tree, this problem can be resolved efficiently.

The SA-based algorithm used to solve the contraction path problem employs a score function that is analogous to an energy function in physics. As described in [24], the classical form of the score function is expressed,

$$\log(T_{cc} + \alpha T_{mc}) + \beta \log(T_{sc}), \quad (6)$$

where α is a parameter that adjusts the balance between computing complexity and memory complexity according to the hardware. T_{sc} denotes the size of the largest intermediate tensor, and β is a parameter controlling the fraction of T_{sc} in the score function.

Once the score function for the contraction path finding task has been defined, two further components are necessary to implement an efficient SA-like optimization algorithm: local update and sweep. In spin models, a local update typically involves a single spin flip, while a sweep involves traversing all spins in the system. However, in the context of contraction path finding, a local update is defined as exchanging descendants of the same ancestor vertex in a contraction tree. To restrict the exchange to be non-trivial and local, it is limited to three nearest descendants [24]. This constraint leads to two possible directions to move. An example of a local update in contraction trees is illustrated in Figure 2(d). Here, the original contraction order of three descendants (C, E , and L) is starting the contraction with the former two tensors followed by the contraction of the result with the third tensor. The local update changes the contraction order to contracting the last two tensors first and then contracting with tensor C . As for sweeping in contraction trees, it refers to the process of traversing all vertices from the root to the leaves [27].

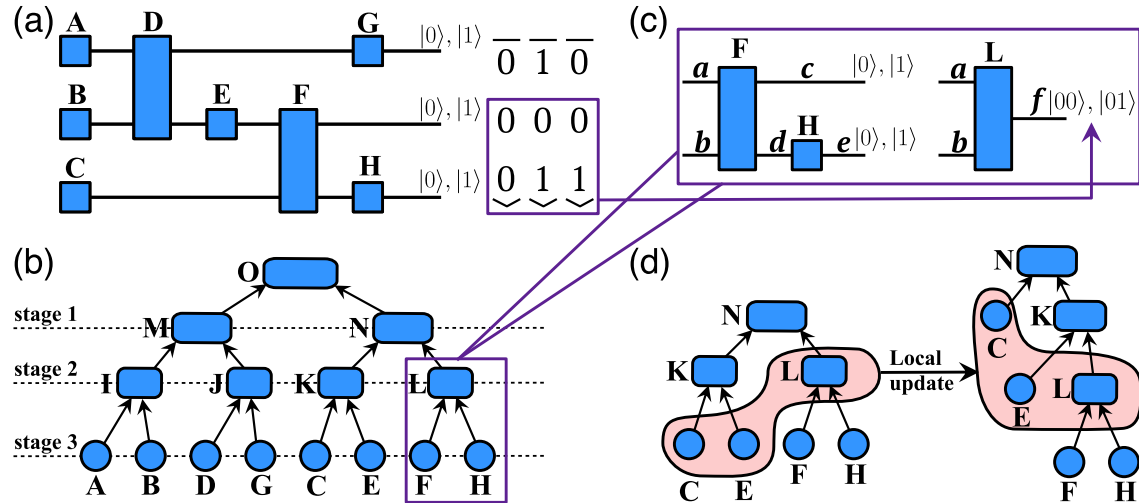


Fig. 2. Overall scheme for the sparse state simulation method. (a) A tensor network that represent a quantum circuit, the aim of the simulation task is calculating the amplitudes of the sparse-state on the right-hand side of the network. (b) A contraction tree represent the unique contraction order of the tensor network in (a). (c) Sparse einsum operation, wherein two tensors with open bonds are contracted, and the merged bond f is calculated based on the sparse-state in (a). (d) A local update that transforms contraction sub-tree from (b) to a new one. The local update area is marked by shaded red.

The size of the largest intermediate tensor in arbitrary tensor network contraction is known to be exponential to the tree-width of the underlying graph [33]. Consequently, executing the entire contraction at once on current computational hardware may be impossible. In such cases, it becomes necessary to slice the entire contraction into smaller sub-tasks that can be executed on available computational resources. The sub-tasks must be designed to

ensure they can be executed within the computational limitations of the hardware. During simulation, these sub-tasks are independent of each other and can be parallelly implemented on different computing devices. This process of parallelization substantially enables larger and more complex tensor networks to be effectively simulated on existing hardware.

The slicing technique is a relatively straightforward approach in tensor network simulation of quantum circuits. As summation indices are typically located at the connections between tensors, slicing involves cutting these connections and fragmenting the tensor network into d smaller pieces, where d is typically equal to 2 in the case of quantum circuits. These smaller pieces have a slightly altered structure than the original network, potentially resulting in a change of the optimal contraction order [11]. Therefore, after each slicing step, the contraction order must be fine-tuned to fit the new tensor network structure, until the largest intermediate tensor can be contained within the computational hardware. This iterative slicing-fine tuning process is referred to as the dynamic slicing process in tensor network contraction by partitioning. The dynamic slicing process is a crucial step in efficiently executing tensor network contractions on existing computational hardware, especially in the context of quantum circuit simulations.

3.3 Sparse-state contraction

Upon determining the contraction order and slicing scheme of the tensor network, the next step in simulation is to perform numerical contraction. Traditional tensor network contractions rely on vanilla einsum or tensordot operations. However, in the sparse-state simulation context, tensor network contractions differ somewhat and require the introduction of "sparse einsum" operations.

The primary distinction arises when two open bonds come together. As mentioned in the preceding section, open bonds in the tensor network simulation of quantum circuits epitomize the distinct layout of the final quantum states. Typically, the bonds of two tensors with differing open bonds are joined through reshape operations into a single entity, merging two indices into one. The dimension of conjoined indices corresponds precisely to the size of the Hilbert space that emerges from the tensor-product of the individual qubits' Hilbert spaces indicated by the open bonds before the merge.

In our task, only bitstrings sampled from quantum experiments are required, making it unnecessary to retain the entire dimension of merged open bonds. To restore the required information from merged open bonds, we utilize bitstring samples to determine the entries to keep while contracting tensors. For instance, in Figure 2(c), when tensors F and H are contracted, c and e , representing open bonds, are merged. To match the sparse-state, which only contains the unique configurations $|100\rangle$, $|101\rangle$, and $|001\rangle$, the dimension of merged bond f should be 2, corresponding to $|00\rangle$ and $|01\rangle$. In terms of an equation, this operation can be expressed as

$$L_{fab} = \text{concat}(\sum_d F_{c=0,abd} H_{e=0,d}, \sum_d F_{c=0,abd} H_{e=1,d}), \quad (7)$$

where the concatenation occurs in the dimension of f , and the subscripts of tensors represent their respective indices. This operation, referred to as "sparse einsum," is essential in simulating quantum circuits since the majority of states that arise in practical simulations are typically sparse.

By adhering to the restriction of the sparse state, composed of bitstring samples, its amplitudes can be obtained through a single tensor network contraction.

4 OPTIMIZATION ON GPU

4.1 Transfer Einsum into GEMM in tensor network

In a contraction tree like Figure 2(b), according to the distance from the final tensor, the tensor contraction can be divided into stage 1, stage 2, etc., with the most time-consuming part concentrated in the stage 1, which is the process of contracting tensors to the stem tensor. As discussed in Section 3.3, the tensor contraction process of the tensor network involves a large number of einsum, batch einsum, and sparse einsum. Therefore, optimizing the contraction of these tensors is crucial for improving the efficiency of the entire tensor network contraction.

Generally speaking, the tensor network can contain hundreds or thousands of tensors. Determining the contraction order and the index arrangement of each contraction is an NP-hard problem. The index arrangement has a significant impact on the efficiency of the computation on the GPU. As mentioned in Section 2.4, when the contracting indices and remaining indices are located in the front and rear parts of the tensor indices after transposition, respectively, the tensor contraction can be represented as a GEMM operation. Therefore, after the tensor contraction path is determined, we can perform index reordering on certain einsums along the critical path to obtain performance benefits at a relatively small cost.

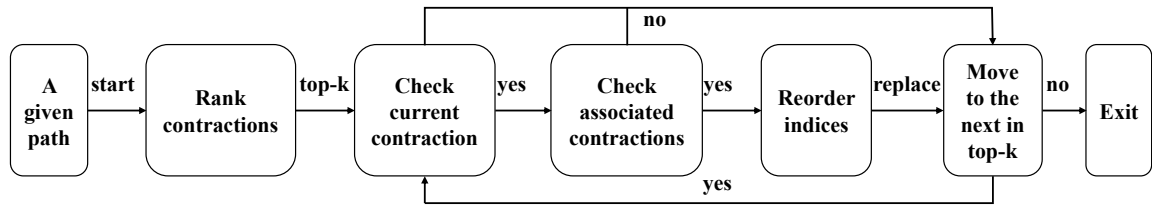


Fig. 3. Reorder indices for top-k contractions in a tensor network.

Figure 3 shows the index reordering process for the determined path, which mainly includes the following parts:

Rank contractions: Rank all contractions based on computing complexity or actual time consumption, and obtain the top-k contractions group with the highest computing complexity or time consumption.

Check current contraction: Starting from the most time-consuming contraction, check whether it is suitable for reordering indices. The criteria for reordering indices are: 1) it has not been modified by other reordering steps; 2) only by modifying the input index order can it form a GEMM expression without modifying the output order of the current contraction. If both are possible, proceed to the next step to check the associated contraction. If not, move on to the next contraction in the top-k group.

Check associated contractions: Here, the associated contractions refer to the contractions related to the two input tensors from the previous step. For example, as shown in Figure 2(b), if the current contraction $O = \text{einsum}(M, N)$ is determined to reorder, then check if the output indices of the associated contractions for $M = \text{einsum}(I, J)$ and $N = \text{einsum}(K, L)$ can be reordered. The criteria for this are that neither of these two contractions has been modified by other reordering steps. If reordering is possible, proceed to reorder the output indices of the relevant contractions. If not, move on to the next contraction in the top-k group.

Reorder indices: If both previous two steps are confirmed to be reordered, then in this step, reorder and replace the indices of the current contraction and associated contractions in the top-k group.

Overall, the index reordering for the top-k contractions is similar to the transpose process in the previously mentioned TTGT algorithm. The difference is that instead of directly transposing tensors at one step, the indices of the output

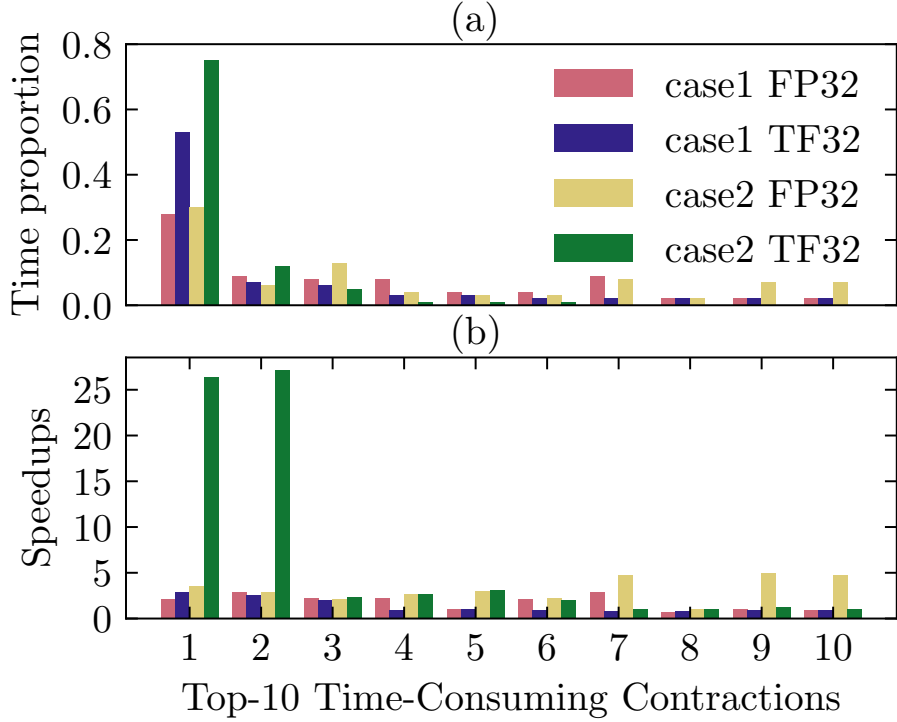


Fig. 4. The time proportion and speedups of transferring einsum to GEMM for the top-10 time-consuming contractions in two tensor network contraction cases.

tensors are reordered according to the order required by the next contractions, thus avoiding additional temporary storage overhead. The cost can be ignored compared to the transposition in TTGT algorithm since it only affects the output of two input tensors. After reordering the indices of the top-k contractions, we can usually make the most time-consuming contractions in the contraction tree a GEMM operation, thereby improving the GPU execution efficiency of the critical contraction. Figure 4 shows two examples of tensor network contractions (i.e., experiments in the Section 5) computed using FP32 and TF32. Figure 4(a) displays the percentage of time spent on the top-10 contractions, which are shown to be the most time-consuming ones. It is evident that the computation is concentrated on a few contractions. Figure 4(b) shows the speedups of transforming the top-10 contractions from Einsum to GEMM, which ranges from 1x to 26x.

Furthermore, as mentioned in Section 3.3, the tensor network contraction for the sampling problem includes sparse einsum operations, which are often the most time-consuming part of the entire contraction tree contraction process. To the authors' knowledge, this operation is not supported natively by any existing computing library to this date. A compromise implementation is to perform slicing first, extract the required tensors from the original tensor for aggregation, and then perform batched einsum calculation. This method has two main drawbacks: 1) slicing increases the amount of data to be read, and the slicing time may become the bottleneck of the entire sparse einsum calculation; 2) it increases the memory requirement for storing intermediate sliced tensors, which is not friendly to quantum circuit simulation with limited memory resources. In this routine, after the above reordering step, since the

`cublasGemmBatchedEx()` API in cuBLAS supports passing separate pointers for each matrix of the batched GEMM input, we can directly transfer the reordered sparse einsum into batched GEMM. This completely eliminates the slicing process for computing sparse einsum. In Figure 4, the two most time-consuming contractions are both sparse einsums. It can be seen that after reordering and using batched GEMM, their calculation efficiency can be improved up to 26 times.

As quantum circuits become deeper and more complex, tensor contractions become denser, making the optimization strategy more effective.

4.2 Extended precision

In scientific computing, including quantum circuit simulations, significant decrease in calculation accuracy is usually unacceptable. As a result, the use of low-precision Tensor Cores to accelerate computations directly is often not feasible, despite their high throughput capabilities. In order to address this issue, CUTLASS introduced a new implementation in version 2.8 using three TF32 Tensor Core instructions to emulate the FP32 operations [35]. Compared to native FP32 operations, the 3xTF32 method achieves between 2-3x speedup while maintaining the accuracy.

$$\begin{aligned}
 X_{\text{big}} &= \text{float_to_tf32}(X), \\
 X_{\text{small}} &= \text{float_to_tf32}((X - \text{float}(X_{\text{big}}))), \\
 A * B + C &= (A_{\text{big}} + A_{\text{small}}) * (B_{\text{big}} + B_{\text{small}}) + C \\
 &\approx A_{\text{big}} * B_{\text{small}} + A_{\text{small}} * B_{\text{big}} + A_{\text{big}} * B_{\text{big}} + C.
 \end{aligned} \tag{8}$$

The 3xTF32 method is shown in Equation 8. The FP32 matrix elements of matrices A and B are split into large and small parts which are represented as TF32 data. For A matrix element a , the large part a_{big} is the direct lossy conversion from the FP32 data to TF32, while the small part a_{small} is residual of the conversion from a to a_{big} . In this way, the original multiplication and addition operation is split into four multiplication and addition operations. The operation of two residuals can usually be ignored, so the calculation is approximated as three TF32 Tensor Core operations. The use of 3xTF32 expands the significant digits of TF32, and obtains significant digits similar to FP32, thereby improving the calculation accuracy. From the perspective of speedup, using 1xTF32 can obtain 8x speedup compared to FP32, while using 3xTF32 can theoretically obtain 8/3, which is close to 2.3x speedup.

We extend the above method to FP16 and BF16 precision to implement the 3xFP16/3xBF16 method. As shown in Table 1, the precision of the FP16 data type is equivalent to the TF32, but the exponent part can only represent data with a small dynamic range. The BF16 data type has the same dynamic range as the TF32 data type, but lower data precision. Therefore, if the actual data range of the application is within the dynamic range of FP16, 3xFP16 can obtain the same calculation accuracy as 3xTF32, but at a 2x speedup theoretically. When the data exceeds the dynamic range of FP16, we can also consider using 3xBF16 to obtain a trade-off between speedup and accuracy.

We extended CUTLASS's support to 3xFP16 and 3xBF16 following the 3xTF32 method. To simplify the complexity of precision testing, we use vector dot products to study the effects of different methods on the resulting accuracy. This is because both einsum and GEMM can be seen as composed of non-interfering basic vector dot products. We use the data range from 1e3 to 1e-7, which we refer to as FP16 range later in the remainder of this article, to test the calculation accuracy of different calculation methods.

Figure 5 shows the relative error comparison of 1xTF32, 3xBF16, 3xTF32, 3xFP16 and FP32 under FP16 range. It can be concluded that the errors calculated by 3xTF32 and FP32 are roughly the same, the error of 1xTF32 is significantly larger than that of 3xTF32, and the error of 3xBF16 is between the two. According to the previous discussion, under the

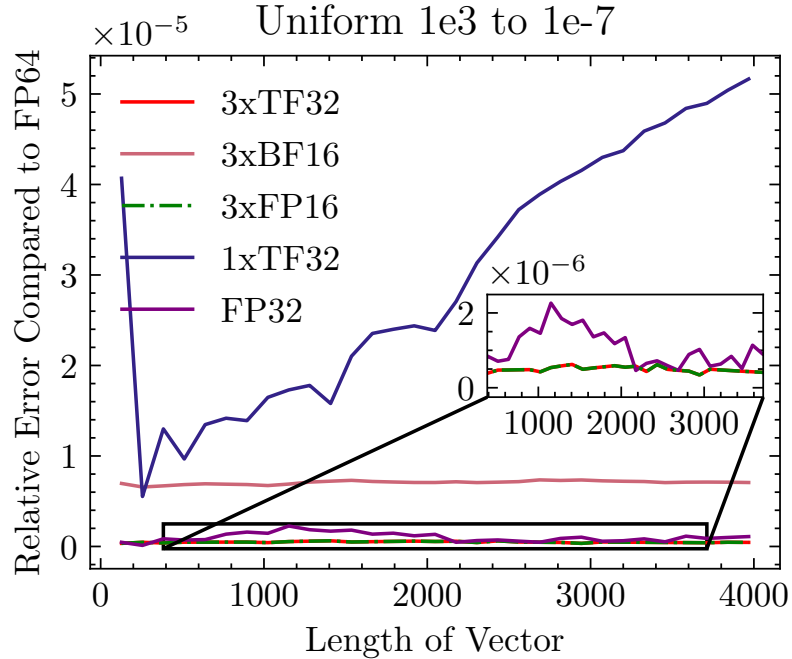


Fig. 5. Relative Error comparison of FP32, 1×TF32, 3×FP16, 3×BF16, 3×TF32 on $10^{+3} \sim 10^{-7}$.

FP16 range, the $3 \times$ FP16 method should obtain the same calculation accuracy as $3 \times$ TF32. The zoomed view in Figure 5 shows that the errors of $3 \times$ TF32 and $3 \times$ FP16 are exactly the same. They are even better than the calculation accuracy of FP32 in this test. However, $3 \times$ BF16 is limited by the significant digits that BF16 can represent, making its calculation error relatively larger, but still smaller than $1 \times$ TF32.

Through the above experiments, it can be concluded that the $3 \times$ TF32 method can obtain calculation accuracy equivalent to that of FP32. If the data range satisfies the FP16 dynamic range, we can directly use the $3 \times$ FP16 method to obtain further acceleration. When the data accuracy exceeds the FP16 dynamic range, the $3 \times$ BF16 method serves as a compromise between performance and calculation accuracy. Additionally, projecting data onto the FP16 data representation range through dynamic scaling can also be an option.

4.3 Mixed precision

A single Tensor Core instruction (TF32/FP16/BF16) can offer high peak performance for floating-point calculations, albeit with lower precision. On the other hand, multiple Tensor Core instructions ($3 \times$ TF32/FP16/BF16) can provide higher precision, but the peak performance may only reach up to one-third or less of a single Tensor Core instruction. The precision requirements of quantum circuit simulation vary for different types of computing tasks. Therefore, it is crucial to explore the balance between precision and performance according to the specific computing task's requirements to maximize the computing power of the GPU's Tensor Cores.

In this section, we utilized the F_7 verification problem of a relatively small-scale Sycamore quantum circuit instance with 45-qubit and 14-cycle to show that by adjusting the computation precision of different parts in the tensor network

Table 2. Comparison of F_l and time for 45-qubit 14-cycle circuit with different precision

| Precision | F_l | $\epsilon_{F_l}(\%)$ | Speedups |
|-----------|--------------------|----------------------|----------|
| FP64 | 0.004753936 | 0.0 | 1 |
| FP32 | 0.004753947 | 2.28E-4 | 1.49 |
| 3×TF32 | 0.004730105 | 0.5 | 2.57 |
| TF32 | 0.004288435 | 9.79 | 3.22 |

simulation it is possible to achieve a balance between computation efficiency and accuracy. The problem involves calculating amplitudes for 2^{20} sampled bitstrings and contains 2^{14} sub-tasks after slicing, where each sub-task performs 280 contraction steps. We performed the tensor network contraction using various precision formats, namely FP64, FP32, 3×TF32, and TF32, to calculate the F_l results at these precisions. Table 2 presents the impact of different precisions on the accuracy and performance of the final result. As expected, the performance improves with increasing precision while the accuracy decreases. Notably, the result of 3×TF32 is acceptable, with only a 0.5% difference from the FP64 result. However, the TF32 result is clearly unacceptable, with a 9.79% error. Hence, we investigated the effects of different ratios of TF32 and 3×TF32 on accuracy and performance by adjusting the ratio based on the computing complexity in tensor network contraction calculation. We did not adopt 3×FP16/BF16 because they are not supported by the latest version of cuTensor.

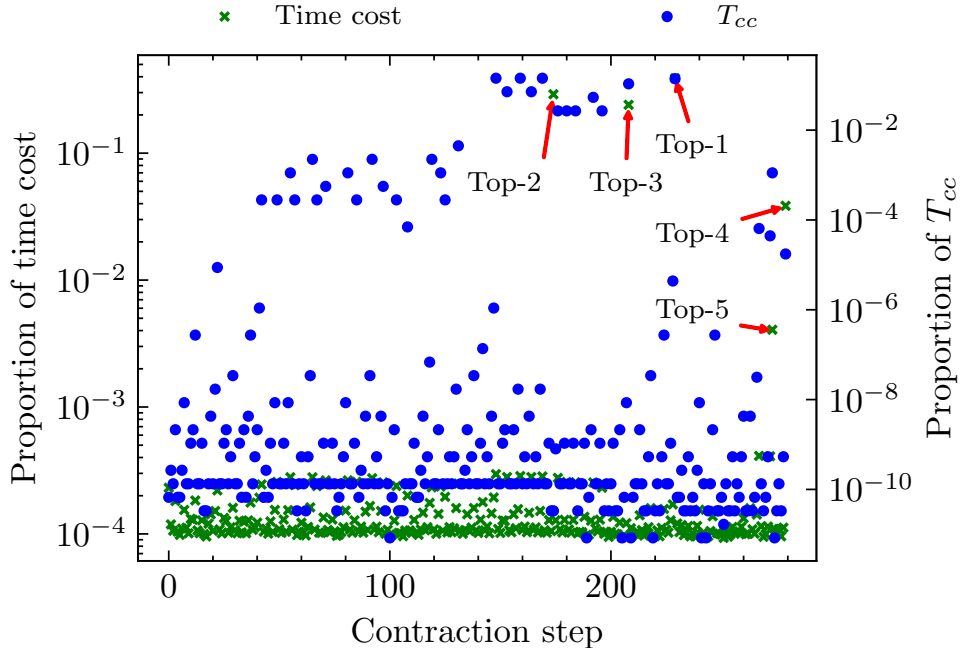


Fig. 6. Time cost and computing complexity for each contraction step, the top-5 most time-consuming contractions are highlighted.

Based on the characteristics of tensor network contraction, the computation is concentrated in the later stages of the contraction process, as shown in Figure 6. In order to investigate the impact of different TF32 ratios on computation

efficiency, we first sorted all contractions according to the actual computation time, and then gradually converted the computation precision from $3 \times \text{TF32}$ to TF32 starting from the most time-consuming contraction. We used ϵ_{L2^2} , which is the relative error for the squared L2-norm of the resulting tensor

$$\epsilon_{L2^2} = |L2^2 - L2^{2'}|/L2^2, \quad (9)$$

to quantitatively analyze the effect of different TF32 ratios on the result accuracy. The squared L2-norm was used since Equation 2 shows that $p_U(x_i)$ calculates the probability of a complex vector x , and can be expressed as the square of the L2-norm of x . Thus, Equation 2 can be written as:

$$F_l = 2^N \sum_{i=1}^m p_U(x_i)/m - 1 = L2(x)^2 2^N / m - 1. \quad (10)$$

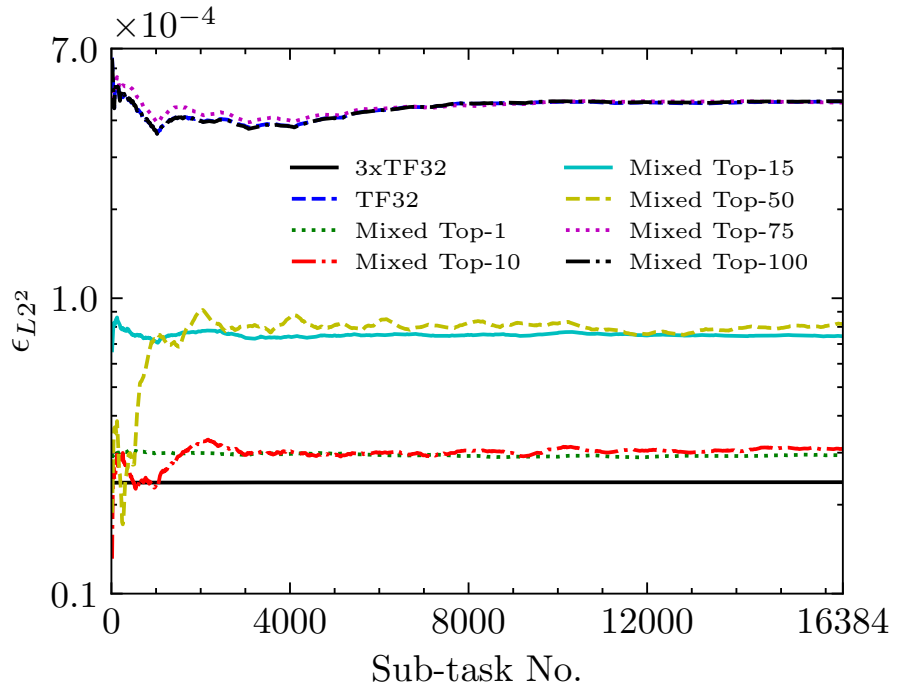


Fig. 7. The relative errors of the squared L2-norm for different mixed.

Figure 7 illustrates the impact of different TF32 ratios on ϵ_{L2^2} . It is noticeable that as the replacement ratio increases, ϵ_{L2^2} also increases gradually. After replacing $3 \times \text{TF32}$ computation entirely with TF32 , ϵ_{L2^2} increased by 20 times. Additionally, it can be observed that for a particular TF32 ratio, as the number of sub-tasks increases, ϵ_{L2^2} displays a stable trend. Consequently, once ϵ_{L2^2} becomes stable, the final error of F_l can be determined because the relative error ϵ_{F_l} of F_l can be expressed as ϵ_{L2^2} :

$$\epsilon_{F_l} = |F_l - F'_l|/F_l = \epsilon_{L2^2}(1 + F_l)/F_l. \quad (11)$$

Table 3. Accumulated T_{cc} ratio replaced, relative time to that with TF32, and relative error after replacing precision of the top-k contractions from $3 \times$ TF32 to TF32.

| Top-k | T_{cc} ratio | Relative time | ϵ_{L2^2} |
|-------|----------------|---------------|-----------------------|
| 0 | 0 | 1.34 | 2.38×10^{-5} |
| 1 | 0.14 | 1.26 | 2.94×10^{-5} |
| 10 | 0.68 | 1.10 | 3.08×10^{-5} |
| 50 | ~ 1 | ~ 1.00 | 8.20×10^{-5} |
| 280 | 1 | 1 | 4.63×10^{-4} |

Table 4. Computing time and sustained FLOPS with/without optimization and on different precisions on 53-qubit 18-cycle Sycamore RCS experiments verification task.

| Precision/Optimization | FP32/No | FP32/Yes | Mixed/Yes |
|----------------------------|---------|----------|-----------|
| Time per sub-task (sec.) | 14.32 | 9.99 | 3.62 |
| Time all tasks (GPU hours) | 33,368 | 23,278 | 8,435 |
| Sustained FLOPS (TFLOPS) | 5.46 | 7.82 | 21.57 |

Table 3 presents the impact of varying TF32 ratios on computation time and ϵ_{L2^2} , showing that the error increases as more contractions use TF32. Notably, the calculation is concentrated on a few contractions, and reducing the precision of key contractions from $3 \times$ TF32 to TF32 can considerably decrease computation time while keeping the overall accuracy within an acceptable range. For instance, replacing the top-10 contractions with TF32 reduces the relative TF32 computation time from 1.34 to 1.1, with a minor increase in ϵ_{L2^2} from 2.38×10^{-5} to 3.08×10^{-5} .

5 EXPERIMENTS

In this section, we present a demonstration of the effectiveness of the sparse-state tensor network simulation method in both verification and bounded LXEB fidelity simulation tasks of Google’s RCS experiment [6] using the optimization methods mentioned previously. The circuits and bitstring samples employed in this study were retrieved from [34]. Our experimental work was carried out on a DGX-A100 [36] equipped with eight NVIDIA A100-SXM-80GB GPUs. The experiment used CUDA version 11.8, cuTensor version 1.6 with $3 \times$ TF32 support, and cuBLAS version 11.11. Each A100 GPU executed partial sub-tasks independently, and the final outcome was the sum of the resulting tensors.

5.1 18-cycle verification task

To limit computational resource requirements to a reasonable size, we calculated amplitudes for 2^{20} out of 2.5 million bitstrings sampled from 53-qubit 18-cycle circuits, the estimated LXEB fidelity for all sampled bitstrings is 0.356%.

In the simulation optimization of the 18-cycle circuit, we first checked the top-10 contractions based on the principles outlined in Section 4.1. The total computing complexity of these top-10 contractions accounts for 70.3% of the entire tensor network computing complexity. After checking, a total of 50.62% of the computing complexity can be transferred from einsum into GEMM. In order to further improve the computational efficiency of the GEMM part, we also applied the mixed precision method to change the computational precision of the GEMM part from $3 \times$ TF32 to TF32. For comparison, we calculated 1 million sub-tasks using FP32, $3 \times$ TF32, and mixed methods, and then compared the relative errors of L2-norm squared. As shown in Figure 8(a), it can be seen that the ϵ_{L2^2} of $3 \times$ TF32 and mixed methods are stable with respect to the results of FP32, and are 3.36×10^{-5} and 5.7×10^{-5} , respectively.

By implementing the aforementioned optimizations, we successfully calculated exact bitstring amplitudes for 2^{20} in 8435 GPU hours. Table 4 displays that the final optimized version with mixed precision yielded a 3.96-fold acceleration as compared to the non-optimized FP32 version. This acceleration is attributable to two factors: firstly, the optimization of transferring sparse einsum to a pure FP32 GEMM operation allowed for a 30% reduction in computational time, and secondly, the utilization of mixed precision resulted in a time reduction factor of 2.76.

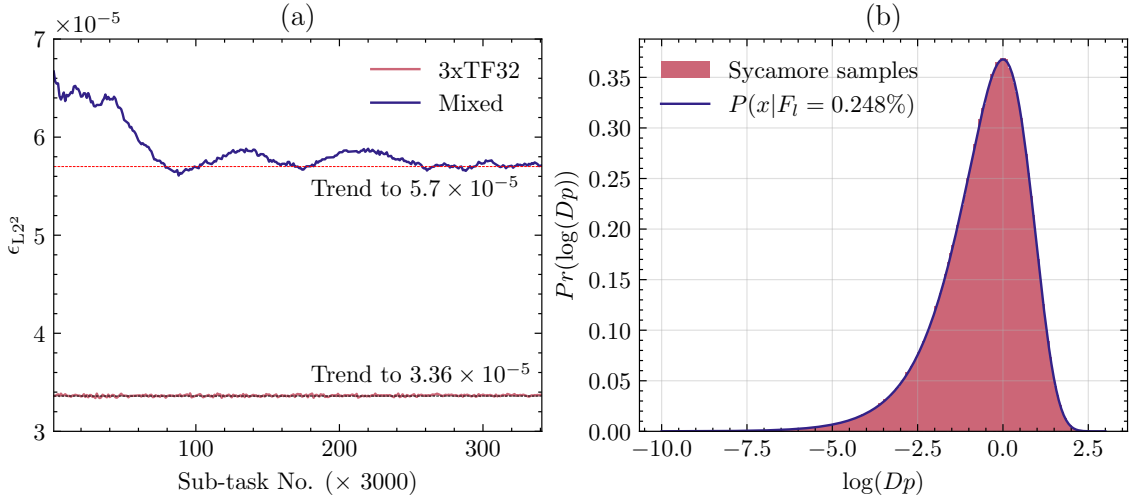


Fig. 8. (a) Relative Errors of squared L2-norm with 3xTF32 and mixed precision. (b) Histogram of the bitstring probability distribution over 2^{20} bitstring samples of 53-qubit 18-cycle Sycamore circuit. The purple line in (b) represents the theoretical distribution with 0.248% LXEB fidelity.

We computed the LXEB fidelity of 2^{20} bitstrings using Equation 2. The resulting value was $F_l = (0.248 \pm 0.00571)\%$, where the error was estimated using Equation 11. Figure 8(b) illustrates the corresponding histogram of the bitstring probabilities, while the theoretical probabilistic density function [6] of the sampled bitstrings is

$$P(x|F_l) = (1 + F_l(e^x - 1))e^{x - e^x}, \quad (12)$$

where $x \equiv \log(Dp)$ and $D = 2^N$. The consistency between the numerical experiments and theoretical distribution indicates that the 2^{20} bitstrings of the 53-qubit 18-cycle do follow the Porter-Thomas distribution with estimated LXEB fidelity. While our calculated LXEB value does not exactly match Google's estimate, it is important to note that we only utilized approximately 42% of the entire sample and there were ten circuit instances for the 18-cycle case. Thus, from a statistical point of view, our results provide validation for the output of Sycamore circuits with 53 qubits and 18 cycles.

5.2 20-cycle verification and simulation task

In order to compare our results with other simulation methods and implementations on different platforms, we will also examine the 20-cycle case. Considering the non-interacting sub-tasks in tensor network simulation, it is relatively straightforward to estimate the running time of a small fraction of sub-tasks and extrapolate it to the entire simulation.

We employed our algorithm to estimate the computational cost and time required to compute all 3 million sampled bitstrings from the 53-qubit 20-cycle Sycamore circuits. This task was accomplished using a CPU-based method [28]

Table 5. Verification details about 53-qubit 20-cycle Sycamore circuits.

| | |
|--|-----------------------|
| Overall T_{cc} | 9.15×10^{22} |
| Number of sub-tasks | 2^{30} |
| Largest intermediate tensor | 32 GB |
| One sub-task time (FP32 before optimization) | 17.39 sec. |
| One sub-task time (FP32 after optimization) | 11.28 sec. |
| One sub-task time (mixed after optimization) | 4.22 sec. |

Table 6. Cost of bounded LXEB fidelity (0.224%) simulation task of 53-qubit 20-cycle Sycamore RCS experiments.

| Methods | Pan et al.[41] | Kalachev et al.[25] | Our |
|------------------|-----------------------|----------------------|-----------------------|
| Overall T_{cc} | 6.19×10^{18} | 2.2×10^{19} | 2.56×10^{19} |
| Device | V100-32GB | V100-16GB | A100-80GB |
| GPU hours | 4,604 | 10,800 | 2,819 |
| Bitstring num | 2^{20} | 2 million | 3 million |

that utilized the entire supercomputer consisting of 41,932,800 cores with a single-precision peak performance of 1.5 EFLOPS, and the final validation task was completed in 203 hours. A summary of our verification details is presented in Table 5. Based on our computing complexity and efficiency, if we use the same single-precision peak performance as the CPU-based method, the required computing time would be 43.7 hours, only 21.5% of the CPU-based approach. Moreover, if mixed precision is allowed, which does not introduce significant errors, the required computing time is further reduced to 16.4 hours, which is only 8% of the supercomputer’s time.

We compared our simulation approach with other GPU-based simulation techniques for the task of generating bitstring samples with bounded fidelity in the RCS experiments on the 53-qubit 20-cycle Sycamore circuits. In the tensor network simulation of RCS experiments, all sub-tasks are orthogonal to each other [32, 41]. Thus, summing the fraction equal to the LXEB value of overall sub-tasks results in the bitstring samples with the same LXEB fidelity. Therefore, we can estimate the resources required for the simulation task when compared to others by multiplying a specific LXEB fidelity by our computational cost.

Table 6 provides a comprehensive comparison of our simulation cost with the results reported in [25, 41]. Notably, our simulations generate a higher number of bitstrings, resulting in a computational cost that is up to 4.13x higher than the other two methods. However, our method’s simulation cost is significantly lower, comprising only 61% of the cost reported in [41] and 26% of the cost reported in [25]. With the same overall computing complexity (T_{cc}), the simulation could be accelerated by 6.78 and 4.48 times, respectively.

6 CONCLUSIONS AND OUTLOOK

In this article, we propose several optimizations for tensor network simulation methods to accelerate sampling-based quantum experiments on large-scale, highly entangled quantum circuits using modern GPUs while maintaining simulation fidelity. Our optimizations include optimizing computing kernels and data precision. We transfer sparse einsum operations into GEMM operations, reducing the time for the most time-consuming part of the overall simulation. To meet the high precision requirements of the LXEB verification task, we use extended precision to mitigate inaccuracies caused by using computing precision in customized processing units designed to accelerate tensor operations. In addition, we use mixed precision to accelerate large tensor operations in the simulation, and validate that this usage only has

negligible effects on the final results. Combining these optimizations, we successfully verified RCS experiments on 53-qubit 18-cycle Sycamore quantum circuits, sampling over 1 million bitstrings with a 3.93x performance improvement compared to the non-optimized version. We also estimated the computational costs of the bounded LXEB simulation task and the verification task of 53-qubit 20-cycle Sycamore RCS experiments using our algorithms, and found that our final results were superior to other CPU and GPU-based methods.

For future work, we suggest exploring two avenues to optimize tensor network simulations. The first is to optimize the index arrangement of the tensors involved from the perspective of improving the overall efficiency of tensor network contraction. This can bring a more regular memory access pattern without affecting the overall computational complexity, and can better make use of the full power of the Tensor Core. The second direction involves re-scaling the quantum circuit data. Due to the unitary nature of quantum circuits and the exponential size of the Hilbert space, the floating-point numbers inside tensors tend to become increasingly smaller during contraction. To fully utilize the throughput of low floating-point precision, a possible solution is to re-scale the tensors at the beginning or during the tensor network contraction process.

ACKNOWLEDGMENTS

We thank Daochen Shi, Rita Zhang, and Guofeng Zhou for helpful discussions. A python implementation that can reproduce the optimizations achieved in this paper is available at [20]. The contraction order is generated by package ArTensor [40]. P.Z. acknowledges the WIUCASICTP2022 grant and Project 11747601 and 11975294 of NSFC.

REFERENCES

- [1] Scott Aaronson and Alex Arkhipov. 2011. The computational complexity of linear optics. In *Proceedings of the forty-third annual ACM symposium on Theory of computing*. 333–342. <https://doi.org/10.4086/toc.2013.v009a004>
- [2] Scott Aaronson and Lijie Chen. 2016. Complexity-Theoretic Foundations of Quantum Supremacy Experiments. *arXiv:1612.05903 [quant-ph]* (Dec. 2016). arXiv:1612.05903 [quant-ph]
- [3] Scott Aaronson and Shih-Han Hung. 2023. Certified randomness from quantum supremacy. *arXiv preprint arXiv:2303.01625* (2023).
- [4] Dorit Aharonov, Xun Gao, Zeph Landau, Yunchao Liu, and Umesh Vazirani. 2022. A Polynomial-Time Classical Algorithm for Noisy Random Circuit Sampling. *arXiv:arXiv:2211.03999*
- [5] Juan Miguel Arrazola and Thomas R Bromley. 2018. Using Gaussian boson sampling to find dense subgraphs. *Physical review letters* 121, 3 (2018), 030503.
- [6] Frank Arute, Kunal Arya, Ryan Babbush, Dave Bacon, Joseph C. Bardin, Rami Barends, Rupak Biswas, Sergio Boixo, Fernando G. S. L. Brandao, et al. 2019. Quantum Supremacy Using a Programmable Superconducting Processor. *Nature* 574, 7779 (Oct. 2019), 505–510. <https://doi.org/10.1038/s41586-019-1666-5>
- [7] Boaz Barak, Chi-Ning Chou, and Xun Gao. 2020. Spoofing linear cross-entropy benchmarking in shallow quantum circuits. *arXiv preprint arXiv:2005.02421* (2020). <https://arxiv.org/abs/2005.02421>
- [8] Roorzbeh Bassirian, Adam Boulard, Bill Fefferman, Sam Gunn, and Avishay Tal. 2021. On certified randomness from quantum advantage experiments. *arXiv preprint arXiv:2111.14846* (2021).
- [9] Sergio Boixo, Sergei V. Isakov, Vadim N. Smelyanskiy, Ryan Babbush, Nan Ding, Zhang Jiang, Michael J. Bremner, John M. Martinis, and Hartmut Neven. 2018. Characterizing Quantum Supremacy in Near-Term Devices. *Nature Physics* 14, 6 (June 2018), 595–600. <https://doi.org/10.1038/s41567-018-0124-x>
- [10] Sergey Bravyi, Martin Suchara, and Alexander Vargo. 2014. Efficient Algorithms for Maximum Likelihood Decoding in the Surface Code. *Physical Review A* 90, 3 (Sept. 2014), 032326. <https://doi.org/10.1103/PhysRevA.90.032326> arXiv:1405.4883
- [11] Jianxin Chen, Fang Zhang, Cupjin Huang, Michael Newman, and Yaoyun Shi. 2018. Classical Simulation of Intermediate-Size Quantum Circuits. *arXiv:1805.01450 [quant-ph]* (May 2018). arXiv:1805.01450 [quant-ph]
- [12] Song Cheng, Chenfeng Cao, Chao Zhang, Yongxiang Liu, Shi-Yao Hou, Pengxiang Xu, and Bei Zeng. 2021. Simulating noisy quantum circuits with matrix product density operators. *Physical Review Research* 3, 2 (2021), 023005. <https://doi.org/10.1103/PhysRevResearch.3.023005>
- [13] Jack Choquette, Wishwesh Gandhi, Olivier Giroux, Nick Stam, and Ronny Krashinsky. 2021. Nvidia a100 tensor core gpu: Performance and innovation. *IEEE Micro* 41, 2 (2021), 29–35.
- [14] Anne C Elster and Tor A Haugdahl. 2022. Nvidia hopper gpu and grace cpu highlights. *Computing in Science & Engineering* 24, 2 (2022), 95–100.

- [15] Edward Farhi, Jeffrey Goldstone, and Sam Gutmann. 2014. A quantum approximate optimization algorithm. *arXiv preprint arXiv:1411.4028* (2014).
- [16] Richard P Feynman. 1982. Simulating Physics with Computers. *International Journal of Theoretical Physics* 21, 6/7 (1982). <https://doi.org/10.1007/BF02650179>
- [17] Xun Gao, Marcin Kalinowski, Chi-Ning Chou, Mikhail D. Lukin, Boaz Barak, and Soonwon Choi. 2021. Limitations of Linear Cross-Entropy as a Measure for Quantum Advantage. *arXiv:2112.01657 [cond-mat, physics:quant-ph]* (Dec. 2021). arXiv:2112.01657 [cond-mat, physics:quant-ph]
- [18] Johnnie Gray and Stefanos Kourtis. 2021. Hyper-Optimized Tensor Network Contraction. *Quantum* 5 (March 2021), 410. <https://doi.org/10.22331/q-2021-03-15-410> arXiv:2002.01935
- [19] Lov K Grover. 1996. A fast quantum mechanical algorithm for database search. In *Proceedings of the twenty-eighth annual ACM symposium on Theory of computing*. 212–219.
- [20] Hanfeng Gu. 2023. *Sycamore verification*. Retrieved October, 2023 from https://github.com/Hanfeng23/Sycamore_verification
- [21] Craig S Hamilton, Regina Kruse, Linda Sansoni, Sonja Barkhofen, Christine Silberhorn, and Igor Jex. 2017. Gaussian boson sampling. *Physical review letters* 119, 17 (2017), 170501. <https://doi.org/10.1103/PhysRevLett.119.170501>
- [22] Cupjin Huang, Fang Zhang, Michael Newman, Xiaotong Ni, Dawei Ding, Junjie Cai, Xun Gao, Tenghui Wang, Feng Wu, Gengyan Zhang, Hsiang-Sheng Ku, Zhengxiong Tian, Junyin Wu, Haihong Xu, Huanjun Yu, Bo Yuan, Mario Szegedy, Yaoyun Shi, Hui-Hai Zhao, Chunqing Deng, and Jianxin Chen. 2021. Efficient Parallelization of Tensor Network Contraction for Simulating Quantum Computation. *Nature Computational Science* (Sept. 2021). <https://doi.org/10.1038/s43588-021-00119-7>
- [23] Antti-Pekka Hyhnninen and Dmitry I Lyakh. 2017. cutt: A high-performance tensor transpose library for cuda compatible gpus. *arXiv preprint arXiv:1705.01598* (2017).
- [24] Gleb Kalachev, Pavel Panteleev, and Man-Hong Yung. 2021. Recursive Multi-Tensor Contraction for XEB Verification of Quantum Circuits. *arXiv:2108.05665 [quant-ph]* (Aug. 2021). arXiv:2108.05665 [quant-ph]
- [25] Gleb Kalachev, Pavel Panteleev, PengFei Zhou, and Man-Hong Yung. 2021. Classical Sampling of Random Quantum Circuits with Bounded Fidelity. *arXiv:2112.15083 [quant-ph]* (Dec. 2021). arXiv:2112.15083 [quant-ph]
- [26] Stefanos Kourtis, Claudio Chamon, Eduardo Mucciolo, and Andrei Ruckenstein. 2019. Fast Counting with Tensor Networks. *SciPost Physics* 7, 5 (Nov. 2019), 060. <https://doi.org/10.21468/SciPostPhys.7.5.060>
- [27] Jin-Guo Liu, Xun Gao, Madelyn Cain, Mikhail D. Lukin, and Sheng-Tao Wang. 2022. Computing solution space properties of combinatorial optimization problems via generic tensor networks. <https://doi.org/10.48550/ARXIV.2205.03718>
- [28] Yong Liu, Yaqian Chen, Chu Guo, Jiawei Song, Ximin Shi, Lin Gan, Wenzhao Wu, Wei Wu, Haohuan Fu, Xin Liu, Dexun Chen, Guangwen Yang, and Jiangang Gao. 2022. Validating Quantum-Supremacy Experiments with Exact and Fast Tensor Network Contraction. *arXiv:arXiv:2212.04749*
- [29] Yong (Alexander) Liu, Xin (Lucy) Liu, Fang (Nancy) Li, Haohuan Fu, Yulng Yang, Jiawei Song, Pengpeng Zhao, Zhen Wang, Dajia Peng, Huarong Chen, Chu Guo, Heliang Huang, Wenzhao Wu, and Dexun Chen. 2021. Closing the "Quantum Supremacy" Gap: Achieving Real-Time Simulation of a Random Quantum Circuit Using a New Sunway Supercomputer. In *Proceedings of the International Conference for High Performance Computing, Networking, Storage and Analysis*. ACM, St. Louis Missouri, 1–12. <https://doi.org/10.1145/3458817.3487399>
- [30] Lars S Madsen, Fabian Laudenbach, Mohsen Falamazri Askarani, Fabien Rortais, Trevor Vincent, Jacob FF Bulmer, Filippo M Miatto, Leonhard Neuhaus, Lukas G Helt, Matthew J Collins, et al. 2022. Quantum computational advantage with a programmable photonic processor. *Nature* 606, 7912 (2022), 75–81. <https://doi.org/10.1038/s41586-022-04725-x>
- [31] Stefano Markidis, Steven Wei Der Chien, Erwin Laure, Ivy Bo Peng, and Jeffrey S Vetter. 2018. Nvidia tensor core programmability, performance & precision. In *2018 IEEE international parallel and distributed processing symposium workshops (IPDPSW)*. IEEE, 522–531.
- [32] Igor L. Markov, Aneeqa Fatima, Sergei V. Isakov, and Sergio Boixo. 2018. Quantum Supremacy Is Both Closer and Farther than It Appears. *arXiv:1807.10749 [quant-ph]* (Sept. 2018). arXiv:1807.10749 [quant-ph]
- [33] Igor L. Markov and Yaoyun Shi. 2008. Simulating Quantum Computation by Contracting Tensor Networks. *SIAM J. Comput.* 38, 3 (Jan. 2008), 963–981. <https://doi.org/10.1137/050644756> arXiv:quant-ph/0511069
- [34] John M. Martinis et al. 2022. *Quantum supremacy using a programmable superconducting processor, Dryad, Dataset*. Retrieved March, 2023 from <https://doi.org/10.5061/dryad.k6t1rj8>
- [35] NVIDIA. 2019. *CUTLASS 2.8*. Retrieved December 20, 2021 from <https://github.com/NVIDIA/cutlass/discussions/385>
- [36] NVIDIA. 2020. *NVIDIA DGX A100 System Architecture*. Retrieved January, 2023 from <https://images.nvidia.com/aem-dam/en-zz/Solutions/data-center/dgx-a100/dgxa100-system-architecture-white-paper.pdf>
- [37] NVIDIA. 2023. CUBLAS LIBRARY user guide v12.1. *CUDA Toolkit Documentation* (2023).
- [38] Hiroyuki Ootomo, Hidetaka Manabe, Kenji Harada, and Rio Yokota. 2023. Quantum Circuit Simulation by SGEMM Emulation on Tensor Cores and Automatic Precision Selection. *arXiv preprint arXiv:2303.08989* (2023).
- [39] Hiroyuki Ootomo and Rio Yokota. 2022. Recovering single precision accuracy from Tensor Cores while surpassing the FP32 theoretical peak performance. *The International Journal of High Performance Computing Applications* 36, 4 (2022), 475–491.
- [40] Feng Pan. 2023. *artensor*. Retrieved October, 2023 from <https://github.com/Fanerst/artensor>
- [41] Feng Pan, Keyang Chen, and Pan Zhang. 2022. Solving the Sampling Problem of the Sycamore Quantum Circuits. *Phys. Rev. Lett.* 129, 9 (2022), 090502.
- [42] Feng Pan and Pan Zhang. 2022. Simulation of Quantum Circuits Using the Big-Batch Tensor Network Method. *Physical Review Letters* 128, 3 (Jan. 2022), 030501. <https://doi.org/10.1103/PhysRevLett.128.030501>

- [43] Alberto Peruzzo, Jarrod McClean, Peter Shadbolt, Man-Hong Yung, Xiao-Qi Zhou, Peter J Love, Alán Aspuru-Guzik, and Jeremy L O'brien. 2014. A variational eigenvalue solver on a photonic quantum processor. *Nature communications* 5, 1 (2014), 4213.
- [44] Charles E Porter and Robert G Thomas. 1956. Fluctuations of nuclear reaction widths. *Physical Review* 104, 2 (1956), 483.
- [45] John Preskill. 2018. Quantum computing in the NISQ era and beyond. *Quantum* 2 (2018), 79.
- [46] Elina Robeva and Anna Seigal. 2017. Duality of Graphical Models and Tensor Networks. *arXiv:1710.01437 [quant-ph, stat]* (Oct. 2017). arXiv:1710.01437 [quant-ph, stat]
- [47] Peter W Shor. 1994. Algorithms for quantum computation: discrete logarithms and factoring. In *Proceedings 35th annual symposium on foundations of computer science*. Ieee, 124–134.
- [48] Paul Springer, Paolo Bientinesi, and Gerhard Wellein. 2019. *High-performance tensor operations: tensor transpositions, spin summations, and tensor contractions*. Technical Report. Fachgruppe Informatik.
- [49] Paul Springer and Chen-Han Yu. 2019. cuTENSOR: High-Performance CUDA Tensor Primitives. In *NVIDIA GPU Technology Conference 2019*.
- [50] Jyothi Vedurada, Arjun Suresh, Aravind Sukumaran Rajam, Jinsung Kim, Changwan Hong, Ajay Panyala, Sriram Krishnamoorthy, V Krishna Nandivada, Rohit Kumar Srivastava, and P Sadayappan. 2018. TTLG—an efficient tensor transposition library for GPUs. In *2018 IEEE International Parallel and Distributed Processing Symposium (IPDPS)*. IEEE, 578–588.
- [51] Yulin Wu, Wan-Su Bao, Sirui Cao, Fusheng Chen, Ming-Cheng Chen, Xiawei Chen, Tung-Hsun Chung, Hui Deng, Yajie Du, Daojin Fan, Ming Gong, et al. 2021. Strong Quantum Computational Advantage Using a Superconducting Quantum Processor. *Physical review letters* 127, 18 (2021), 180501.
- [52] Han-Sen Zhong, Hui Wang, Yu-Hao Deng, Ming-Cheng Chen, Li-Chao Peng, Yi-Han Luo, Jian Qin, Dian Wu, Xing Ding, Yi Hu, et al. 2020. Quantum computational advantage using photons. *Science* 370, 6523 (2020), 1460–1463. <https://doi.org/10.1126/science.abe8770>
- [53] Yiqing Zhou, E. Miles Stoudenmire, and Xavier Waintal. 2020. What Limits the Simulation of Quantum Computers? *Physical Review X* 10, 4 (Nov. 2020), 041038. <https://doi.org/10.1103/PhysRevX.10.041038>
- [54] Qingling Zhu, Sirui Cao, Fusheng Chen, Ming-Cheng Chen, Xiawei Chen, Tung-Hsun Chung, Hui Deng, Yajie Du, Daojin Fan, Ming Gong, Cheng Guo, et al. 2022. Quantum Computational Advantage via 60-Qubit 24-Cycle Random Circuit Sampling. *Science bulletin* 67, 3 (2022), 240–245.

A RESEARCH METHODS

A.1 Unifying tensor network simulation methods into sparse-state simulation

In the tensor network simulation of quantum circuits, there are typically three categories of simulation: single amplitude, full state, and subspace simulation. For single amplitude cases, only the amplitude of a single bitstring is of interest. This bitstring is re-expressed as a product state, and then added to the end of the quantum circuit to construct a closed tensor network. The resulting tensor network is then repeatedly prepared to obtain amplitudes for different bitstrings using the single amplitude simulation method [33]. In contrast, full state simulation aims to obtain all amplitudes associated with the entire Hilbert space without setting any constraint in the final state. In this case, all bonds in the final state will be open and the contraction of such tensor network will output a 2^N vector which represents all amplitudes in the Hilbert space. However, the memory requirement of this approach is exponential in the number of qubits, rendering it feasible only for quantum circuits with a small number of qubits. Subspace sampling lies between these two approaches. In subspace simulation, the final state is partially closed by applying product tensors to qubits that are not of interest [22, 42]. This allows the amplitudes of the opened Hilbert subspace to be directly obtained by contraction. Subspace sampling is mainly used to obtain samples from quantum circuits with a large number of qubits, where the final state cannot be stored by the available computational resources. In such cases, the state of the closed qubits is randomly chosen and a bitstring is sampled from the opened subspace for further experimentation.

The main difference between the three tensor network simulation methods in quantum circuits is the level of restriction placed on the final state. In single amplitude simulation, the restriction is maximal, as the final state is only allowed to represent a single bitstring. In full state simulation, there are no restrictions on the final state and the entire information of the Hilbert space can be computed. The amount of restriction placed on the final state depends on the size of the circuit and the computational resources. The resulting tensor networks of these three methods are either closed tensor networks or tensor networks with few open bonds. The contraction of such tensor networks is typically ordinary and can be translated into a sequence of einsum equations.

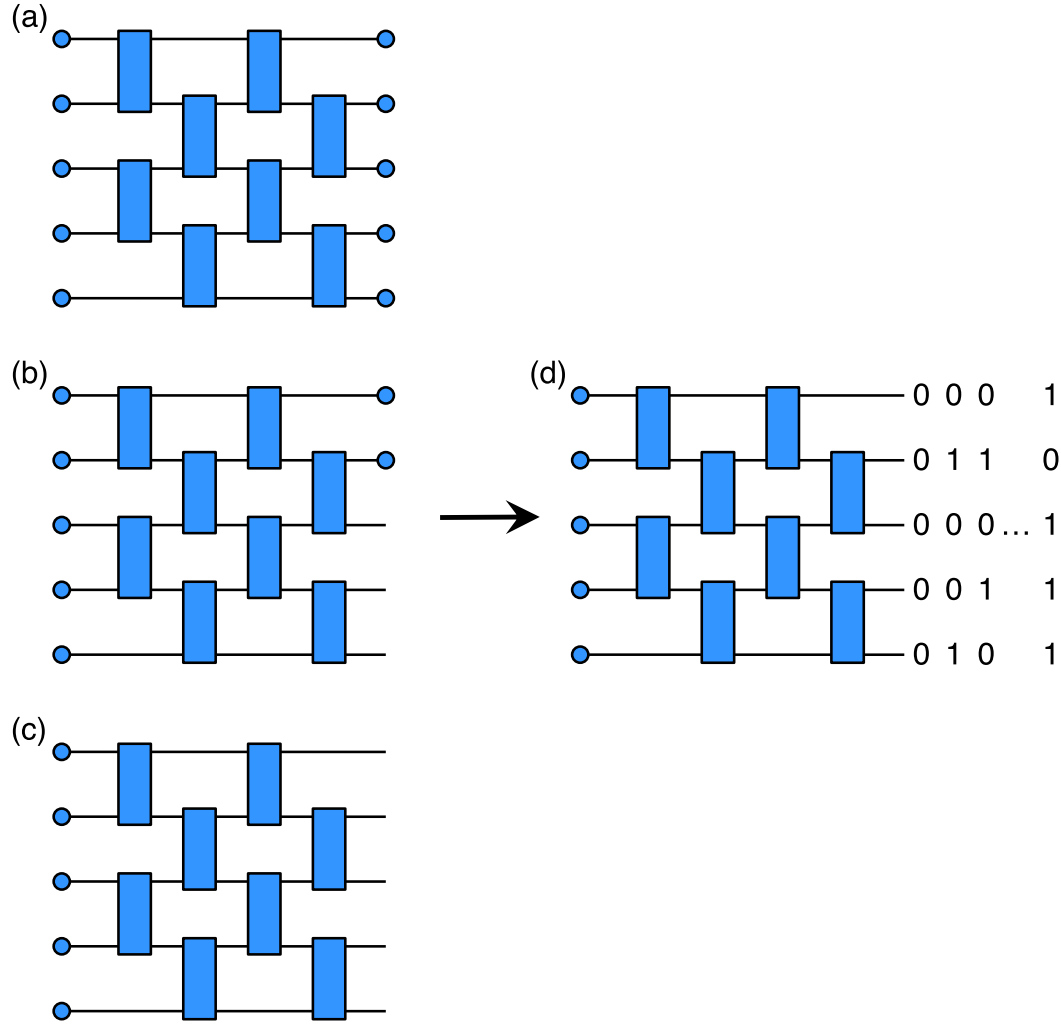


Fig. 9. Unification of three traditional tensor network simulation methods into the sparse-state simulation.

In the main article, we used a different method called sparse-state simulation proposed in [24, 28, 41] that is designed to calculate the amplitudes of multiple bitstrings in one tensor network contraction. Compared to the above three methods, sparse-state simulation adds a different kind of final state restriction, which only allows the final state to be the configuration in bitstring samples. This restriction acts as a boundary condition onto the final state and guides the open bond of qubits and when these bonds merge together.

In Figure 9, we show that the sparse-state tensor network simulation framework unifies the above three methods. For single amplitude simulation, there will be only one state in the sparse-state boundary condition; thus, the number of unique configurations for each open bond merging will be 1. For full-state simulation, the final sparse-state boundary condition will be all states in the Hilbert space, which means that during each merging, the operation will always

be a tensor product, and no index alignments are needed. And for subspace simulation, the circumstances will be a combination of the previous two cases. For qubits closed, the number of unique configurations will be 1, while for qubits opened, the number of unique configurations will be the number of states in such Hilbert subspace.

Since this method is so flexible and can encompass all previous cases, one may wonder why we called it the "sparse-state" simulation method. For the NISQ era, the number of qubits in quantum devices is large, which is beyond the full-state simulation capability of classical computers. At the same time, the number of sampled bitstrings from the quantum experiments will also be limited to a relatively small fraction of the entire Hilbert space because it is impossible to repeat the quantum experiments exponentially many times. Thus, the samples will definitely be a sparse state, and to calculate the probabilities of these samples, the boundary condition onto the final state will only be a constant number. Therefore, for the simulation of such typical quantum experiments, the overall method is dubbed sparse-state simulation.

A.2 Balanced indices

Finally, in the optimization process, we found that although some einsum operations can be transferred into GEMM operation, they cannot fully tap into the computational efficiency of the GPU. Further analysis revealed that this is caused by an imbalance between the contracted indices and the remaining indices. When an einsum is transferred into a GEMM(e.g., $C_{mn} = A_{mk}B_{kn}$), its contracted indices can be equivalent to k in GEMM, and the remaining indices can be equivalent to m and n , i.e., $m = \prod_{i=1}^{d_A} \text{len}(\alpha_i) / \prod_{i=1}^{d_S} \text{len}(\delta_i)$, $n = \prod_{i=1}^{d_B} \text{len}(\beta_i) / \prod_{i=1}^{d_S} \text{len}(\delta_i)$ and $k = \prod_{i=1}^{d_S} \text{len}(\delta_i)$ in Equation 3. When the dimensions m or n of the matrix are smaller than a certain value and there is a significant difference between them, the lower arithmetic intensity results in lower computational efficiency. As a result, the time for accessing matrices is much greater than the time for computing. When the dimension k is small, global memory latency is more severe because pipelined parallelism is not well-suited in the k direction. Therefore, in practical applications, it is necessary to try to keep m , n , and k as similar or as large as possible. Figure 10 compares the actual relative execution time of different shapes of GEMM using Tensor Cores. The base shape for comparison is $32768 \times 2 \times 2$. It can be observed that when m and n are fixed, k should be equal to or greater than 64 to fully utilize Tensor Cores. Similarly, when k is fixed, m or n should be greater than or equal to 32 to fully utilize Tensor Cores. If m or n is less than 32, the closer the values are, the more efficient the Tensor Cores calculation will be. This shows that the matrix size needs to reach a certain threshold to fully utilize the computational power of Tensor Cores. To achieve this, we incorporated positive feedback into the path search algorithm. This resulted in a more balanced ratio, which significantly improves the efficiency of transferred GEMM calculations. Additionally, it increases the computational efficiency of more balanced metrics for einsums that cannot be transferred to GEMM.

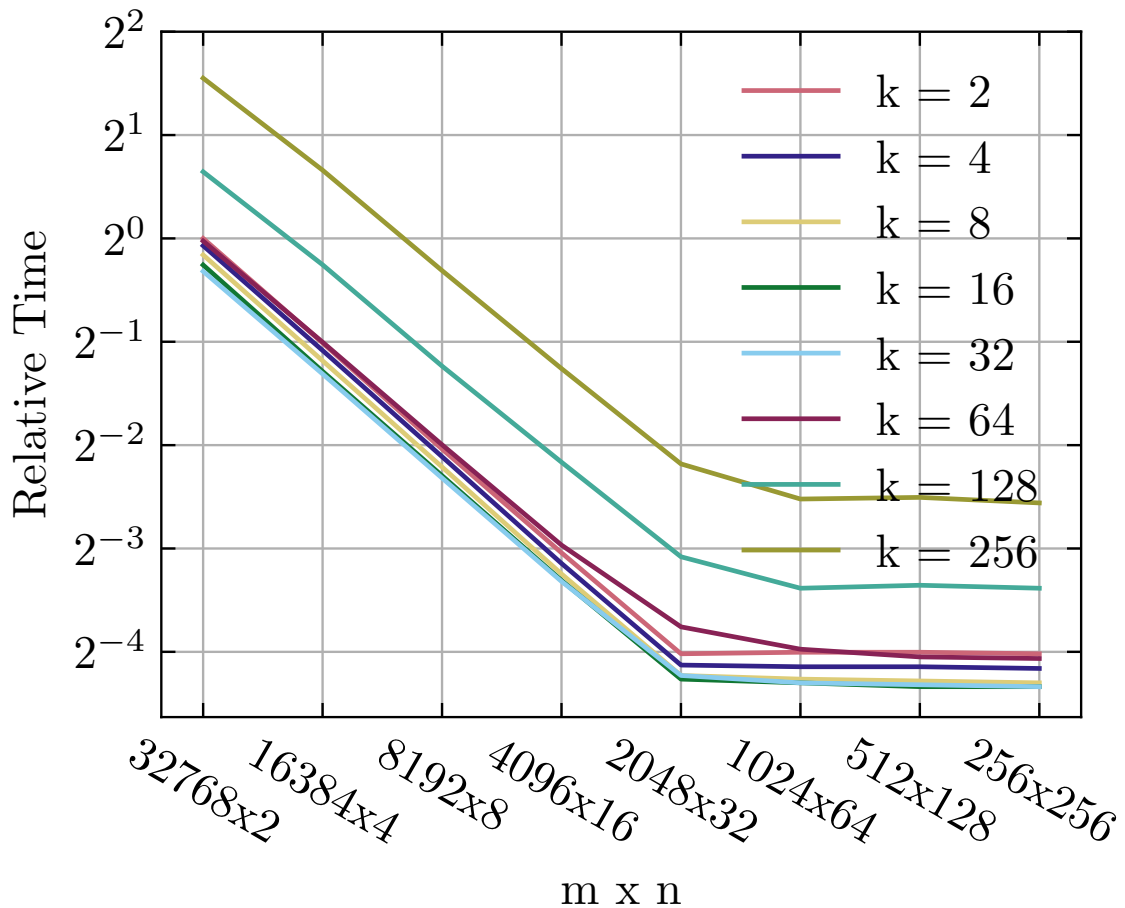


Fig. 10. Comparison of actual execution time for batched GEMM with different shapes using TF32. The baseline shape for time is $1024 \times 32768 \times 2 \times 2$ (batch size $\times m \times n \times k$), and the API being tested is *cublasGemmBatchedEx()*.